https://doi.org/10.5194/egusphere-2025-3403
Preprint. Discussion started: 7 August 2025

Impacts of Source Regions and Atmospheric Transport on Physical Properties of Black Carbon and Tracer Ratios over the Yellow Sea: Evidence from Multi-Seasonal Airborne Observations

Naki Yu[1], Hee-Jung Yoo[2], Sangmin Oh[2], Yongjoo Choi[3], Sunran Lee[2], Sumin Kim[2], Saehee Lim[1,4,*]

[1]Department of Environmental & IT Engineering, Chungnam National University, Daejeon, 34134, Republic of Korea
[2]Global Atmospheric Watch and Research Division, National Institute of Meteorological Sciences, Jeju, 63568, Republic of Korea
[3]Department of Environmental Science, Hankuk University of Foreign Studies, Yongin, 17035, Republic of Korea
[4] Department of Environmental Engineering, Chungnam National University, Daejeon, 34134, Republic of Korea

Correspondence to: Saehee Lim (saehee.lim@cnu.ac.kr)

Abstract. Both size and mixing state of Black carbon (BC) are critical climate-relevant physical parameters. It remains a challenge for ambient measurements to characterize their variability across different atmospheric conditions particularly in outflow regions. To investigate how BC's physical properties are determined in source regions and altered during transport, we conducted 23 flight measurements of BC, CO, and CO_2 over the Yellow Sea from 2021 to 2022. The refractive BC mass concentration (M_{rBC}) varied by up to two orders of magnitude between near sea surface and around 5 km above sea level, and Planetary Boundary Layer height-dependency of M_{rBC} was stronger in winter than in spring. Smallest rBC's mass median diameter MMD (163.4 nm) observed in South Korea-sourced air indicated fresh urban emissions, whereas larger MMD, enhanced internal mixing, and higher rBC/CO slopes were exhibited in the air masses from North Korea and China, reflecting additional emissions from biomass and coal combustion. Both MMD and internal mixing tended to decrease with altitude, highlighting the wet scavenging effect during particle transport. When accumulated precipitation exceeded 1 mm, M_{rBC} decreased by more than 50%, with moderate reductions in MMD and internal mixing. As a result, overall BC transport efficiency declined to 1/e within 5.5 days. These findings emphasize the complex effects of source region, seasonality, and wet removal on varying rBC distributions in the outflow region. We believe that these findings offer valuable observational constraints for improving the physical realism of models.

https://doi.org/10.5194/egusphere-2025-3403
Preprint. Discussion started: 7 August 2025

1 Introduction

The pace of recent climate change has intensified, prompting extensive efforts across scientific, political, and societal domains to curb its impacts (IPCC WG1 AR6). However, the nonlinear and interconnected nature of the climate system presents substantial challenges to accurately predicting outcomes and implementing effective mitigation strategies (IPCC WG1 AR6; Steffen et al., 2018). In this regard, short-lived climate forcers (SLCFs), which include species like methane (CH_4), ozone (O_3), and aerosols, are gaining scientific and political attention in addition to long-lived climate forcers (LLCFs) like CO_2. Black Carbon (BC) is a significant SLCF that contributes roughly 0.14 W m^{-2} of radiative forcing. BC is a carbonaceous aerosol that is directly released into the atmosphere from incomplete combustion of biomass, fossil fuels, and biofuels. It absorbs light strongly in the visible and near-infrared spectrum (IPCC WG1 AR6). BC also modifies atmospheric processes indirectly by acting as cloud condensation nuclei (CCN) (Bond et al., 2013; Jacobson, 2014; Kuwata et al., 2008, 2009) and recent studies have reported a linkage between BC and adverse human health effects including cardiovascular and respiratory diseases (Geng et al., 2013; Hvidtfeldt et al., 2019; Kirrane et al., 2019).

Global anthropogenic BC emissions were estimated at 4,741 Gg $year^{-1}$ in 2022, with approximately 49% (2,316 Gg $year^{-1}$) originating from Asia, based on EDGAR v8.1 (Emissions Database for Global Atmospheric Research) inventory (Crippa et al., 2024). Historical trends prior to 2000 show a decline in BC emissions in North America and Europe (Eckhardt et al., 2023), whereas more recent estimates indicate a sustained increase in Asian emissions over the past two decades in ECLIPSE (Evaluating the Climate and Air Quality Impact of Short-Lived Pollutants) inventory (Klimont et al., 2017). While China has remained the largest national contributor in East Asia (~52 % of Asia's emissions in 2015), countries in South Asia and Russia have emerged as increasingly significant contributors to both regional and global BC emissions (Kurokawa and Ohara, 2020; Regional Emission inventory in Asia (REAS) version 3).

Due to their small size typically within the accumulation mode and hydrophobic nature of freshly emitted particles, urban-sourced BC can be transported over long distances, crossing national and even continental boundaries, and impacting remote or polar environments (Deng et al., 2024; Ginot et al., 2014; Lim et al., 2017, 2022). During transport, BC particles undergo aging processes, generally increasing in size via coagulation and becoming more hygroscopic through internal mixing with co-emitted gases and aerosols from combustion sources (Riemer et al., 2010; Utavong et al., 2024; Weingartner et al., 1997; Zuberi et at., 2005). Previous studies have shown that internal mixing and the formation of coatings enhance BC's light absorption by altering refractive properties (Bond et al., 2013; Lack et al., 2009; Liu et al., 2015). Given that both refractive index and the particle's morphology including size, shape, and coating directly determine its light-absorbing ability (Fuller et al., 1999), understanding the chemical and physical nature of BC and its transformation during atmospheric aging is thus essential for characterizing its optical behavior in a regional scale and constraining its representation in models.

Recent aircraft-based observations have revealed diverse vertical and regional characteristics of BC particles. For example, BC particle diameters were found to be smaller near the surface over urban areas (Lamb et al., 2018), whereas in rural regions, BC tended to decrease in size with increasing altitude (Lu et al., 2019). Differences in BC

https://doi.org/10.5194/egusphere-2025-3403
Preprint. Discussion started: 7 August 2025

mass distribution have also reported between the Atlantic and Pacific Oceans (Katich et al., 2018), and substantial removal of BC, up to 98 %, was observed in Asian summer monsoon outflow (Berberich et al., 2025). These findings provide valuable insight into the transport efficiency and the lifetime of BC under real-world atmospheric conditions.

Given the complex influence of combustion on Asian air quality, analyzing the distribution of combustion-derived components can help identify fuel types, combustion efficiency, and removal processes. Carbon monoxide (CO) shares common sources with BC, making the BC/CO ratio a useful indicator of emission characteristics and transport efficiency. The BC/CO ratio is typically higher for biomass and diesel emissions, and lower for urban gasoline combustion, reflecting differences in fuel type and combustion conditions (Bond et al., 2004; Girach et al., 2014; Zhou et al., 2009). Because BC and CO differ in atmospheric lifetime (about a week and a month, respectively), the BC/CO ratio is particularly sensitive to BC removal processes. Kanaya et al. (2016) reported that, at an Asian background site, an accumulated precipitation along trajectory (APT) of 25.5 ± 6.1 mm reduced BC transport efficiency to 1/e. Similarly, Berberich et al. (2025) showed BC is nearly completely removed from uplifted air in Asian summer monsoon outflow, based on BC and CO relationship. In addition, the ratio of CO to CO_2 has been used as an indicator of combustion efficiency at the emission source. High-efficiency sources, such as modern power plants, exhibit CO/CO_2 ratios below 0.1 % (Peischl et al., 2010), whereas low-efficiency combustion, such as biomass burning, results in substantially higher CO/CO_2 ratios (Suntharalingam et al., 2004; Wang et al., 2010). According to KORea-United States-Air Quality (KORUS-AQ) observations, the CO/CO_2 ratio in the Korean outflow typically ranged from 0–2 %, whereas the ratio for air masses originating from outside the region and mainland China exhibited a broader range of 2–4 % (Halliday et al., 2019). Keeping analyzing these tracer ratios is beneficial in monitoring combustion activities in the region.

Most previous aircraft studies over Asia have focused on observations conducted primarily over inland urban areas, with limited coverage of marine or downwind regions. Several aircraft campaigns have targeted the Yellow Sea region of East Asia, including the Aerosol Radiative Forcing in East Asia (A-FORCE; Oshima et al., 2012; March–April 2009), A-FORCE 2013 winter (Kondo et al., 2016; February–March 2013), and the KORUS-AQ (Lamb et al., 2018; from May–June 2016). While these campaigns have provided valuable datasets, most airborne measurements have been limited to short-term, intensive observational periods. This has restricted the ability to comprehensively assess seasonal variability in the region.

To address this limitation, we present results from a series of aircraft BC measurements conducted over the Yellow Sea in multiple seasons, from February 2021 to May 2022. BC data were collected aboard the research platform as part of the Yellow Sea-Air Quality (YES-AQ) campaign. The analysis presented here focuses on vertical and seasonal variations, combustion characteristics related to air mass origins, and the transport efficiency of BC by examining its physical properties in conjunction with tracer ratios.

https://doi.org/10.5194/egusphere-2025-3403
Preprint. Discussion started: 7 August 2025

2 Methodology

2.1 Aircraft Measurements

2.1.1 Overview of Aircraft Measurements

Aircraft measurements were conducted over the Yellow Sea ("YS") between 8 February 2021 and 2 May 2022, using a King Air 350HW (Beechcraft, USA) research aircraft. A total of 23 flights were carried out along a regular flight path spanning latitudes 34.8° N to 37.6° N and longitudes 124.2° E to 127.1° E. The aircraft operated at altitudes ranging from 400 m to 5,000 m to capture the vertical distribution and seasonal variation of BC properties in the region (Fig. 1a). Each flight was labeled as F(flight)+YYMMDD according to the flight date and corresponding flight information is summarized (Table S1). To minimize the influence of aircraft and airport emissions during takeoff and landing, data collected east of 126.5° E were excluded from the analysis.

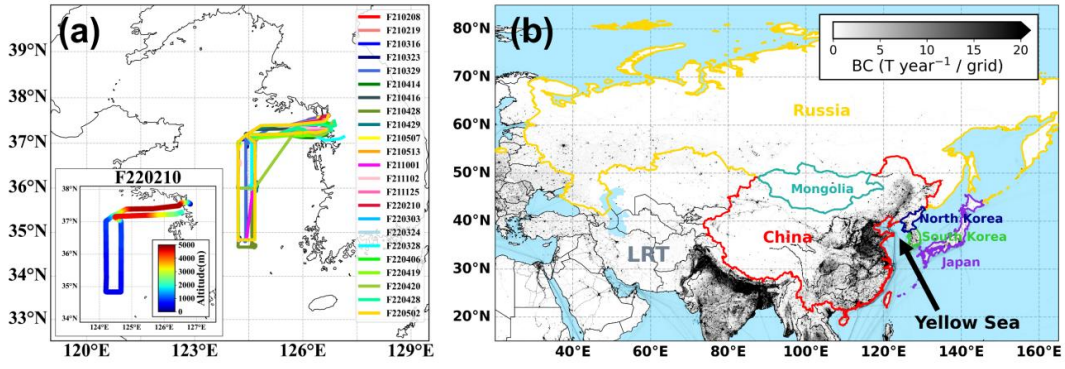

Figure 1. (a) Flight paths for all 23 research flights conducted in this study. All flights departed from the location marked with a star. Different colors represent individual flights. The bottom-left panel shows the flight track for F220210, color-coded by altitude as a representative example of the vertical flight profiles. (b) Black carbon emission rates (tons per year / 0.1° × 0.1° grid cell) with regions where air masses influencing the observations during the aircraft mission (South Korea, North Korea, Japan, China, Mongolia, Russia, and LRT in different colors). BC emissions are sourced and averaged from EDGARv8.1 (Crippa et al., 2024) data for 2021 and 2022.

2.1.2 Planetary boundary layer height

Planetary boundary layer height (PBLH) was defined for each aircraft measurement. Each flight was divided into outbound (start to midpoint) and inbound (midpoint to end) segments as it was cycled. This allowed for distinct PBLH estimates to account for diurnal expansion and contraction. Heffter (1980) proposed that a critical inversion can be identified when the vertical gradient of potential temperature ($\Delta\theta/\Delta z$) exceeds 5 K km^{-1}. Based on this criterion, Halliday et al. (2019) determined PBLH using $\Delta\theta/\Delta z \geq 6$ K km^{-1} and ΔRH (RH_{TOP} - RH_{BASE}) $\leq$ -5 %. Kang et al. (2021) defined the Entrainment Zone (EZ) for each flight as the 90th percentile segment of $\Delta\theta/\Delta z$ (7–13 K km^{-1}). Zhao et al. (2019) set PBLH as the altitude at which $\Delta\theta/\Delta z$ initially reached 5 K km^{-1}.

https://doi.org/10.5194/egusphere-2025-3403
Preprint. Discussion started: 7 August 2025

In this study, $\Delta\theta/\Delta z$ and ΔRH of each layer were calculated in 50-meter altitude bins. For some flights, larger bin sizes (75 m or 100 m) were used to minimize noise in vertical profiles (Figs. S1 and S2). By this approach, the layers satisfying $\Delta\theta/\Delta z > 5$ K km^{-1} were first selected. Among these candidate layers, the one exhibiting the most negative ΔRH value was designated as the EZ. However, for eight flight cases, rather than choosing the layer with the most negative ΔRH, the layer exhibiting the largest positive $\Delta\theta$ value was selected. We considered an upper limit of 1,800 m for base of EZ (=PBLH). Determining PBLH was challenging in some flights mostly due to insufficient data (i.e., F210316 outbound, F210323 inbound, F210329 inbound, F220420 inbound, and F220502 outbound).

2.2 Single particle soot photometer

Single Particle Soot Photometer (SP2, Droplet Measurement Technologies) uses a laser-induced incandescence technique to measure refractory black carbon (rBC) on a particle-by-particle basis (Bond et al., 2013; Petzold et al., 2013; Schwarz et al., 2010; Stephens et al., 2003). The rBC mass is linearly proportional to the signal from the incandescence channels. Aquadag (Acheson Inc.) was used as the calibration standard for the incandescence channels (Gysel et al., 2011; Moteki and Kondo, 2010), with a differential mobility analyzer to select particle diameters ranging from 80 to 480 nm. Polystyrene Latex spheres (Thermo Scientific) with diameters of 200, 240, 300, and 350 nm served as calibration standards for the scattering channels. The SP2 used in this study had a measurement range for rBC of approximately 0.3–130 fg.

The mass-equivalent diameter of rBC (rBC_{MED}) was calculated from particle mass assuming a void-free density of 1.8 g cm^{-3}, and ranged approximately from 70 to 510 nm. (Bond et al., 2013; Moteki and Kondo, 2010). The mass median diameter (MMD) of rBC was determined by fitting a lognormal distribution to the mass size distribution ($dM/dlogD_p$). MMD was calculated as the geometric mean ± geometric standard deviation of 5-minute interval values for each flight, each season, and the entire dataset. In contrast, for specific subsets such as PBL, vertical profiles, Major Regions, and APT conditions, all available data within each category were used to compute a single representative MMD value. The ambient rBC mass concentration (M_{rBC}) dataset was converted to standard temperature and pressure (273.15 K, 1,013 hPa). For purely scattering (rBC-free) particles, the SP2 measurable diameter range was approximately 180–470 nm based on calibrations.

To determine the mixing state of rBC particles based on the SP2 measurements, either the “Delay time” method or the “Leading Edge Only (LEO)-fit” method is commonly used. For bare (uncoated) rBC particles, the peaks of the incandescence and scattering channel signals appear almost simultaneously. However, when rBC particles are coated, a time difference emerges between the two signal peaks, known as “delay time”. This delay time allows for the classification of rBC particles as either “bare or thinly-coated” or “thickly-coated” (Krasowsky et al., 2016; Moteki and Kondo, 2007). In this study, a 1.5 μs delay time threshold was selected from the distribution (Fig. S3) to calculate the number fraction of thickly-coated rBC particles (F_{thick}) among total rBC particles measured, as an indicator of rBC mixing state.

The LEO fitting method quantifies the coating thickness of individual rBC-containing particles by combining SP2 measurement signals with Mie scattering theory (Gao et al., 2007). In the SP2 laser chamber, the coating of an rBC-containing particle evaporates before the particle reaches the beam center, where scattering is maximized. As a

https://doi.org/10.5194/egusphere-2025-3403
Preprint. Discussion started: 7 August 2025

result, the measured scattering signal is lower than that corresponding to the particle's original (pre-evaporation) size. The LEO-fit method reconstructs the scattering signal as if the particle retained its initial shell diameter. This reconstruction is performed by fitting the leading edge of the measured scattering signal, assuming a spherical core-shell morphology with a refractive index of 2.26 + 1.26i for the rBC core (Moteki et al., 2010) and 1.50 + 0.00i for the coating (Taylor et al., 2015; Laborde et al., 2012). In this study, the LEO-fit analysis was applied to rBC particles with diameters (rBC_{MED}) between 140 nm and 220 nm, the range in which the method provides the highest accuracy. The ratio of the reconstructed shell diameter to the measured rBC core diameter ($R_{shell/core}$) was calculated using the optical shell diameter derived from LEO fitting and the rBC_{MED}. All rBC parameters were derived from individual particle-level data (1 Hz resolution) and were aggregated into 10-second intervals for analysis.

2.3 Other measurements

The ambient CO and CO_2 concentrations were measured using Cavity Ring Down Spectroscopy (CRDS, G-2401m, Picarro Inc.). Slopes of rBC versus CO (rBC/CO) and CO versus CO_2 (CO/CO_2) were obtained and analyzed along with rBC physical properties after data was averaged at 10-second intervals (Sect. 3.3). In addition, O_3 (Thermo Scientific model 49i), NO_2 (Thermo Scientific model 42i-TL), SO_2 (Thermo Scientific model 43i-TLE) and aerosol scattering coefficients at a wavelength of 550 nm (TSI model 3563) were measured simultaneously. Meteorological parameters, including air temperature, pressure, wind direction, wind speed, and relative humidity, were measured using the Aircraft Integrated Meteorological Measurement System (AIMMS-20, Aventech Research Inc., Canada). Aircraft position data (latitude, longitude, altitude) were obtained via a Global Positioning System (GPS, C2626, Trimble Inc., USA) in the National Marine Electronics Association (NMEA) format.

2.4 Airmass backward trajectory analysis and source-region identification

Airmass backward trajectories were analyzed using the Hybrid Single Particle Lagrangian Integrated Trajectory (HYSPLIT) model provided by the National Oceanic and Atmospheric Administration (Draxler and Hess, 1997, 1998; Stein et al., 2015) for the flight observations. Using meteorological data from the Global Data Assimilation System (GDAS1, 1° × 1° resolution), airmass trajectories were calculated every 10 seconds for 120 hours, consistent with the atmospheric lifetime of BC. In addition, the accumulated precipitation along trajectory (APT; in mm) was calculated by summing the total precipitation over the 72 hours prior to each trajectory endpoint, in order to investigate the influence of wet removal on rBC properties (Choi et al., 2020b; Kanaya et al., 2016).

To trace the origin of air masses reaching the YS during the aircraft mission, the location of trajectories endpoints for the past 5 days was assigned as potential source region within administrative area maps from Global Administrative Areas (http://gadm.org/). The country most frequently crossed by each trajectory below an altitude of 2.5 km was designated as the origin of that air mass. This classification, referred to as "Major Region", was intended to account for the upward dispersion of surface-emitted pollutants. The Major Region was classified into eight groups: South Korea, North Korea, Japan, China, Mongolia, Russia, long range transport (LRT) and Ocean (Fig. 1b, Table S3, and Fig. S4). For each trajectory, the Major Region was determined using the following criteria: 1) Assign the region crossed most frequently, unless it is Ocean, in which case assign the second most frequently crossed region. 2) If the

https://doi.org/10.5194/egusphere-2025-3403
Preprint. Discussion started: 7 August 2025

most frequent region contributes less than 5 % of endpoints, reassign the Major Region as Ocean to improve classification reliability. 3) If the trajectory crossed only Ocean, assign the Major Region as Ocean. This correction was applied to minimize the oceanic bias that may arise from conducting the flights primarily over the sea.

3 Results and Discussion

3.1 Measurement overview of airborne rBC particles

Throughout the campaign, the YS, located in the mid-latitudes of the Northern Hemisphere, experienced prevalent westerly winds frequently bringing air masses from the continent. Figure 2 presents the statistical distribution of observational parameters for each aircraft measurement. The average rBC mass concentration (M_{rBC}) for individual flights ranged from 58.8 to 671.1 ng m^{-3}, varying by a factor of 10. The overall campaign mean ± standard deviation was 210.7 ± 247.6 ng m^{-3}. The lowest flight-mean M_{rBC} (58.8 ± 104.4 ng m^{-3}; F210316) was comparable to levels measured during aircraft observations over remote regions of continental Europe (~50 ng m^{-3}) (McMeeking et al., 2010), but clearly higher than the those observed over the northern Greenland Sea (7–18 ng m^{-3}; Ohata et al., 2021). In contrast, the highest flight-mean M_{rBC} (671.1 ± 492.3 ng m^{-3}; F220210) was similar to airborne observations over the southeastern Indo-Gangetic Plain (700 ng m^{-3}; Brooks et al., 2019). This level was approximately four times higher than the concentrations reported over the Los Angeles Basin (167 ± 83 ng m^{-3}; Metcalf et al., 2012).

https://doi.org/10.5194/egusphere-2025-3403
Preprint. Discussion started: 7 August 2025

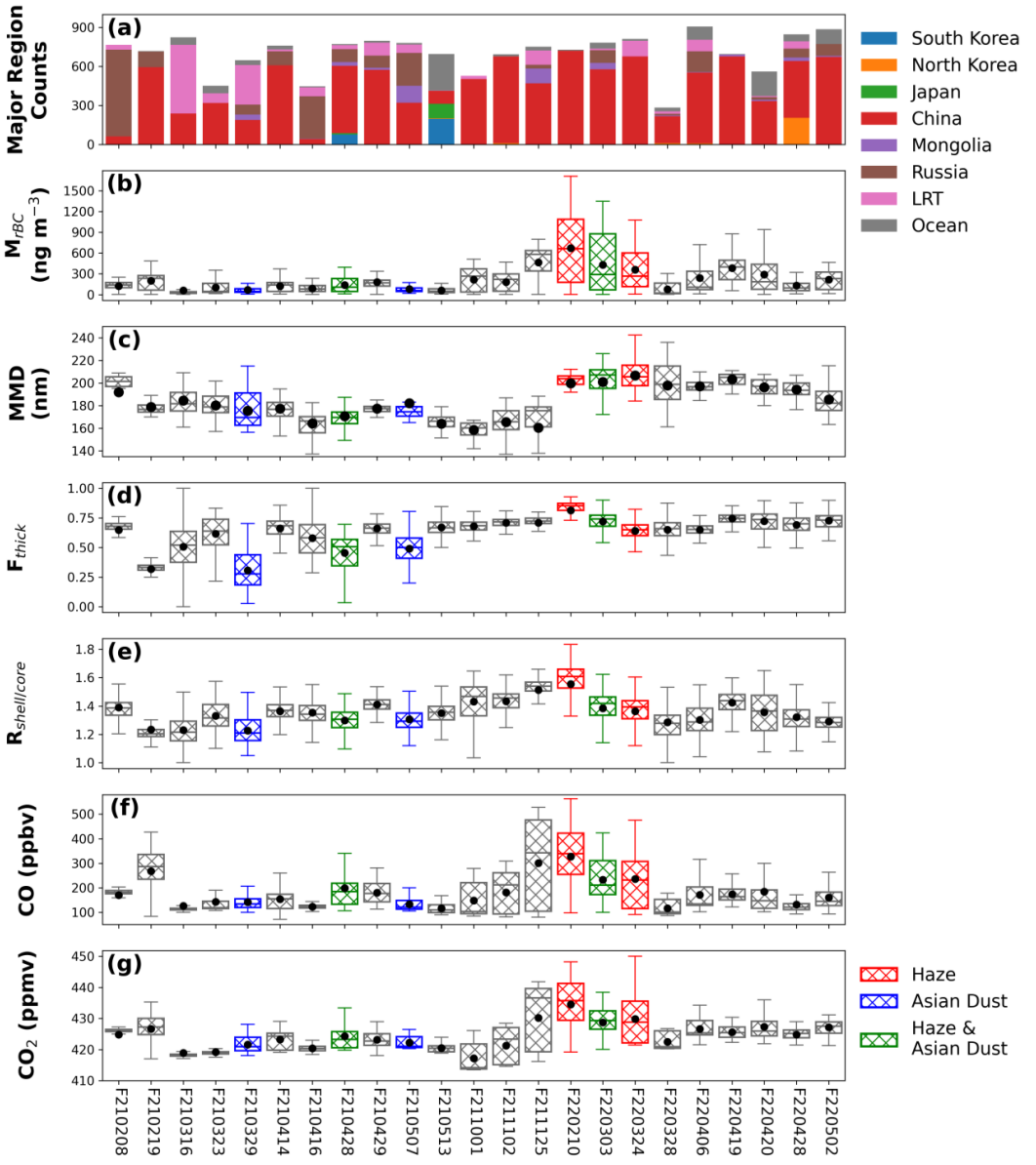

Figure 2. Variations in Major Region contributions and rBC properties for each flight measurement. (a) Number of data points from the Major Regions, (b) rBC mass concentration (M_{rBC}), (c) rBC mass median diameter (MMD), (d) Number fraction of thickly-coated rBC particles (F_{thick}), (e) Range of shell-to-rBC core diameter ($R_{shell/core}$), (f) CO concentration, (g) CO_2 concentration. In box plots, whiskers extend to 1.5 times the interquartile range, boxes represent the 25th to 75th percentiles, and black dots indicate the mean values for M_{rBC}, F_{thick}, and $R_{shell/core}$, while for MMD, they represent the geometric mean. Colors indicate specific events; Haze (red), Asian Dust (blue), and combined Asian Dust & Haze (green).

https://doi.org/10.5194/egusphere-2025-3403
Preprint. Discussion started: 7 August 2025

Ground-based M_{rBC} levels, particularly in urban areas, have generally been much higher than those observed in this study. In the Seoul megacity, summertime M_{rBC} levels were 480 ± 290 ng m^{-3} (Lim et al., 2023), which is roughly twice the mean M_{rBC} observed during this study's aircraft campaign. M_{rBC} measured in Paris, France (900 ± 700 ng m^{-3}), London, UK (900–1,740 ng m^{-3}), Shanghai, China (3,200 ng m^{-3}), and Xi'an, China (~9,900 ng m^{-3}) (Gong et al., 2016; Laborde et al., 2013; Liu et al., 2014; Wang et al., 2014) underscore the substantially elevated concentrations observed in highly urbanized regions. Overall, M_{rBC} levels observed over the YS were, on average, comparable to those over European remote regions, although pollution plumes occasionally elevated its levels as similar as those found over the highly polluted Asian regions.

The 5-minute interval mass median diameter (MMD) of rBC particles varied dynamically ranging from 70 nm to 250 nm. The MMDs of each flight ranged from 158.6 nm to 206.6 nm, with a geometric mean (± geometric standard deviation) of 182.3 ± 1.1 nm across all flights. Previous studies have shown that observed size distributions of rBC generally reflect both emission sources and further particle physical processes (e.g., coagulation and scavenging) in the atmosphere. As examples from ground-based measurements, in Seoul dominated by urban traffic emissions, the MMD was 127 ± 11 nm (Lim et al., 2023), which was smaller than those observed at Jungfraujoch (220–240 nm; Liu et al., 2010) or in biomass-burning plumes over urban Shanghai (~200 nm; Gong et al., 2016). In airborne measurements, MMDs in European remote regions (180–200 nm) were notably larger than those measured in urban outflow (170 ± 10 nm) (McMeeking et al., 2010). Overall, BC's MMDs tend to be larger in remote regions than in urban areas, and biomass-burning emissions generally produce larger MMDs than traffic-related emissions (Ko et al., 2020; Kompalli et al., 2020, Schwarz et al., 2008). While the MMDs observed over the YS thus reflect characteristics of both urban outflow and remote regions, their wide temporal variability suggests clear influences of emissions from diverse emission sources of multiple countries.

The flight-averaged number fraction of thickly-coated rBC particles (F_{thick}) varied greatly from 0.31 to 0.81, with a campaign mean of 0.63 ± 0.16. In urban regions, F_{thick} values are generally below 0.5, as shown by previous measurements in Houston, USA (0.09 ± 0.06; Schwarz et al., 2008) and Los Angeles (0.05 ± 0.02; Krasowsky et al., 2016), and Xi'an, China (0.48 during polluted periods and 0.38 during clean periods; Wang et al., 2014), indicating that roughly more than 50 % rBC particles are bare from fresh emissions. In the PBL over Beijing, F_{thick} was reported to be approximately 0.5 on average (Zhao et al., 2019), which is slightly lower than mean value observed in this study (0.63). Compared to these previous observations, rBC particles over the YS were more aged on average than those over Beijing, while characteristics of urban outflow were revealed. It is noteworthy that two mixing state parameters (F_{thick} and $R_{shell/core}$) showed similar patterns (Fig. 2). Flight-averaged $R_{shell/core}$ values ranged from 1.23 to 1.55, with a campaign mean of 1.35 ± 0.14. As expected, $R_{shell/core}$ values were higher than those observed at urban ground sites, such as 1.25 ± 0.07 in summertime Seoul (Lim et al., 2023) and 1.2 in Beijing from May to June (Liu et al., 2020). However, the degree of BC internal mixing was clearly lower than observed over the Southeast Asia Sea near heavily polluted regions ($R_{shell/core}$ > 2, Kompalli et al., 2021).

Thus, both size distributions (MMD) and mixing state (F_{thick} and $R_{shell/core}$) of rBC particles observed in this study clearly indicate their considerable dependence on the origins and further chemical/physical processes of the air masses during transport to this remote environment.

https://doi.org/10.5194/egusphere-2025-3403
Preprint. Discussion started: 7 August 2025

3.2. Seasonally-varying vertical distributions of rBC properties

3.2.1 Seasonal variability

A total of 23 flights were grouped into five categories by seasons: 2021 Winter (February–March 2021, n=5 flights), 2021 Spring (April–May 2021, n=6 flights), 2021 Autumn (October–November 2021, n=3 flights), 2022 Winter (February–March 2022, n=4 flights), and 2022 Spring (April–May 2022, n=5 flights). Seasonally, M_{rBC} was the highest in winter. In 2022, the winter mean reached 394.3 ± 407.7 ng m^{-3}, followed by autumn (278.9 ± 226.0 ng m^{-3}), and spring (239.0 ± 200.0 ng m^{-3}). In contrast, in 2021, winter and spring exhibited similar mean values, though winter showed greater variability (Table 1). This seasonal pattern is consistent with previous studies in East Asia (Kanaya et al., 2020; Liu et al., 2019, 2022; Lim et al., 2012; Zhao et al., 2013).

The elevation of cold-season M_{rBC} levels reflect the combined effects of increased combustion emissions (e.g., heating) and the synoptic-scale meteorology (predominant westerly winds; Fig. S5), which facilitate the efficient transport of rBC from continental source regions to the YS (Gandham et al., 2022; Zhang et al., 1997). Supporting this, anthropogenic BC emissions (from biofuel and fossil fuel sources) based on the EDGAR v8.1 inventory were highest in 2022 Winter across South Korea and its neighboring countries (North Korea, Japan, China, Mongolia, and Russia; Table S4). The remarkable enhancement of M_{rBC} for 2022 Winter can thus be primarily attributed to intensified regional combustion activities. Furthermore, seasonally-averaged aerosol optical depths (550 nm, DT/DB combined) retrieved along 10-second air mass back trajectories below 2,500 m altitude (Fig. S6) exhibited a consistent seasonal pattern with M_{rBC}, reinforcing the link between regional aerosol loading and combustion activity.

https://doi.org/10.5194/egusphere-2025-3403
Preprint. Discussion started: 7 August 2025

Table 1. Seasonal M_{rBC}, MMD, F_{thick}, and $R_{shell/core}$ (mean ± std). The "FT" in this study is defined as altitudes reaching up to approximately 5 km.

Season		M_{rBC} (ng m^{-3})	MMD (nm)	F_{thick}	$R_{shell/core}$
All (PBLH*: 880±371 m)	all	210.7±247.6	182.3±1.1	0.63±0.16	1.35±0.14
	FT	99.8±134.1	186.2	0.60±0.18	1.32±0.13
	PBL	329.0±264.7	193.2	0.66±0.14	1.39±0.12
2021 Winter (PBLH: 1,011±417 m)	all	112.9±112.3	182.2±1.1	0.48±0.20	1.28±0.14
	FT	36.5±36.7	177.8	0.45±0.22	1.26±0.15
	PBL	215.3±88.9	188	0.53±0.17	1.31±0.10
2021 Spring (PBLH: 685±359 m)	all	110.8±82.0	172.1±1.1	0.58±0.14	1.34±0.08
	FT	97.4±81.5	173.3	0.57±0.14	1.33±0.08
	PBL	128.3±59.1	183.6	0.62±0.14	1.38±0.06
2021 Autumn (PBLH: 1,144±258 m)	all	278.9±226.0	161.9±1.1	0.70±0.09	1.46±0.13
	FT	58.0±85.5	161.6	0.68±0.14	1.37±0.17
	PBL	432.7±162.9	174.6	0.71±0.04	1.51±0.05
2022 Winter (PBLH: 816±316 m)	all	394.3±407.7	201.4±1.1	0.71±0.12	1.40±0.17
	FT	142.1±213.7	204.5	0.68±0.13	1.32±0.16
	PBL	732.4±338.4	207.1	0.76±0.11	1.50±0.14
2022 Spring (PBLH: 873±464 m)	all	239.0±200.0	194.4±1.1	0.70±0.07	1.33±0.11
	FT	169.2±166.0	193.6	0.72±0.08	1.33±0.12
	PBL	250.0±176.9	197.8	0.69±0.07	1.31±0.09

* See Sect. 2.1.2. for the PBLH method.

MMD exhibited seasonal variations similar to M_{rBC}, with the largest rBC size in winter (190.9 ± 1.1 nm), followed by spring (181.3 ± 1.1 nm) and autumn (161.9 ± 1.1 nm). In Asia, the size distribution of rBC particles typically varies seasonally, with larger rBC in cold season than in warm season (Kompalli et al., 2020; Wu et al., 2021; Yang et al., 2019), reflecting an enhanced influence of both biomass burning emissions and long-range transport effects during cold season. The MMD difference was about 20 nm between winter and autumn in this study, comparable to the winter (210–220 nm) to late spring (190–215 nm) difference observed over Beijing (Zhao et al., 2019). This suggests that the seasonal mean MMD difference can be about 20 nm in East Asia, likely stemming from varying major emission sources.

Notably, the particularly low levels of internal mixing and M_{rBC} observed in 2021 Winter were likely associated with reduced anthropogenic activity during the COVID-19 pandemic. In contrast to the relatively consistent seasonal patterns of M_{rBC} and MMD, the mixing state of rBC particles (F_{thick} and $R_{shell/core}$) was more complex

https://doi.org/10.5194/egusphere-2025-3403
Preprint. Discussion started: 7 August 2025

seasonally and displayed pronounced interannual differences. Specifically, in Table 1, F_{thick} was highest in 2022 Winter (0.71 ± 0.12), followed by 2022 Spring (0.70 ± 0.07), 2021 Autumn (0.70 ± 0.09), 2021 Spring (0.58 ± 0.14), and 2021 Winter (0.48 ± 0.20). In contrast, $R_{shell/core}$ was highest in 2021 Autumn (1.46 ± 0.13), followed by 2022 Winter (1.40 ± 0.17), 2021 Spring (1.34 ± 0.08), 2022 Spring (1.33 ± 0.11), and 2021 Winter (1.28 ± 0.14). These patterns suggest that the degree of rBC mixing state is influenced not only by seasonal emission strength but significantly also by meteorological factors operating at both synoptic- and microscale levels. Overall, while the enhanced values of M_{rBC}, MMD, and F_{thick} in winter were commonly found, inter-annual variability merits further discussion in Sect. 3.3.

Figure 3 shows seasonal relationships between planetary boundary layer height (PBLH) and rBC mass concentration (M_{rBC}) within the PBL. Overall, M_{rBC} within the PBL decreased with increasing PBLH, with a more pronounced pattern in winter (-23.4 ng m^{-3}/Δ100 m and -97.6 ng m^{-3}/Δ100 m for 2021 and 2022) than spring (-12.8 ng m^{-3}/Δ100 m and -26.4 ng m^{-3}/Δ100 m for 2021 and 2022). This finding demonstrates the stronger sensitivity of M_{rBC} distribution on PBL development.

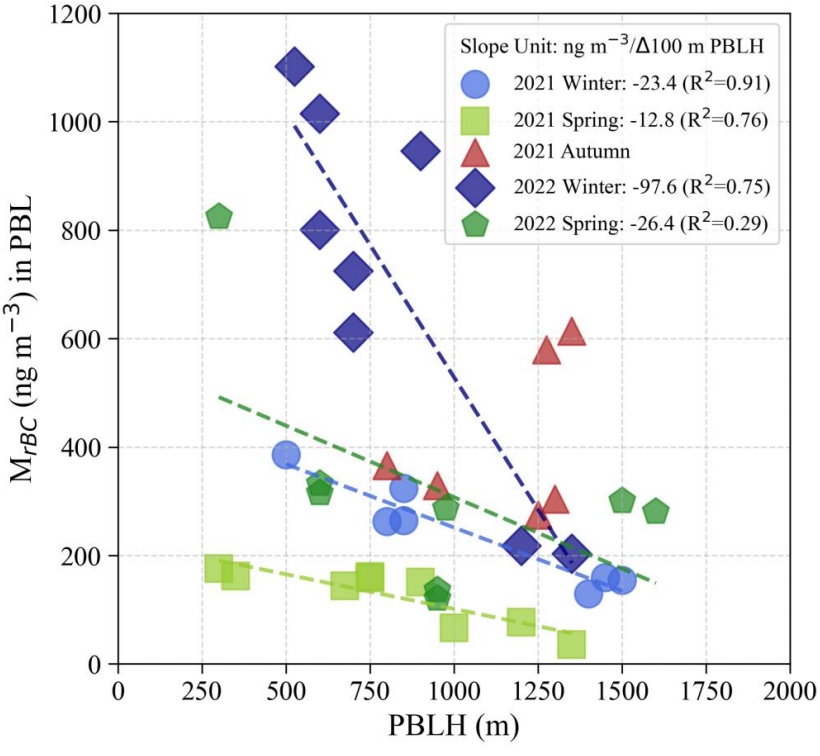

Figure 3. Seasonal relationship between planetary boundary layer height (PBLH) and M_{rBC} within the PBL. Each point represents M_{rBC} averaged within the PBL for either the outbound or inbound segment. Seasonal linear regression lines are shown for Winter and Spring, with slope values expressed in ng m^{-3} per 100 m of PBLH.

https://doi.org/10.5194/egusphere-2025-3403
Preprint. Discussion started: 7 August 2025

3.2.2 Vertical distribution

Figure 4 illustrates seasonally-varying vertical profiles of rBC properties. M_{rBC} exhibited vertical variability spanning up to two orders of magnitude between the near sea surface and 5 km, with an exponential fit of x(y) = 40.5 + 571.6 × exp(-0.87y(km)). Throughout the experiment period, the average M_{rBC} in the PBL (M_{rBC_PBL}; 329.0 ± 264.7 ng m^{-3}) was more than three times greater than that in the lower free troposphere (M_{rBC_FT}; 99.8 ± 134.1 ng m^{-3}, hereafter referred to as "FT"). Seasonally, the M_{rBC_PBL}/M_{rBC_FT} ratios tended to increase from spring (~1.4) to winter (~5.6). Stronger convective uplift effect may partly explain the smaller ratio in spring.

It is noteworthy that both size and internal mixing of rBC decreased with altitude (-4.64 nm km^{-1} for MMD, -0.035 km^{-1} for F_{thick}, and -0.027 km^{-1} for $R_{shell/core}$, respectively). But seasonality was different between two physical properties. The decreasing trends were clearer in spring for MMD (-5.63 nm km^{-1}) but in winter for F_{thick} and $R_{shell/core}$ (-0.045 km^{-1} and -0.034 km^{-1}). Lim et al. (2017) reported that rBC particles preserved in high-altitude (~5.1 km) alpine ice cores exhibited larger MMDs (~200–300 nm) than found on the ground, suggesting that larger rBC particles in the atmosphere are preferentially removed by precipitation and subsequently deposited in ice cores. In a remote marine region far from BC emission sources, markedly thinner coatings of rBC particles were observed, attributing this to preferential scavenging, photolysis, limited precursor supply, and dilution of continental outflow (Kompalli et al., 2021). In line with these studies, our findings reflect that both size and mixing state of rBC particles are strongly sensitive to wet scavenging (cloud and precipitation) at high altitudes (above ~3 km), where rBC particles undergo long-range transport and have a greater likelihood of being scavenged upon transport. It is noteworthy that cloud scavenged larger and mixed rBC particles might have contributed to CCN over YS or potentially further into the Pacific. Yet, the detailed processes governing the observed vertical profiles of rBC physical properties remain unclear.

Also, enhanced photochemical reaction at upper altitude may explain less steeper decreasing pattern of particle internal mixing in spring. As an interesting seasonal feature, 2022 Spring was the only season in which both M_{rBC} and F_{thick} were relatively higher in the FT than in the PBL. Given the high temperature (5.1 ± 10.0 °C) and O_3 concentrations (58.9 ± 9.8 ppbv) in the FT, these conditions likely facilitated enhanced photochemical reactions aloft, promoting rBC coating formation and leading to higher degree of rBC mixing state.

https://doi.org/10.5194/egusphere-2025-3403
Preprint. Discussion started: 7 August 2025

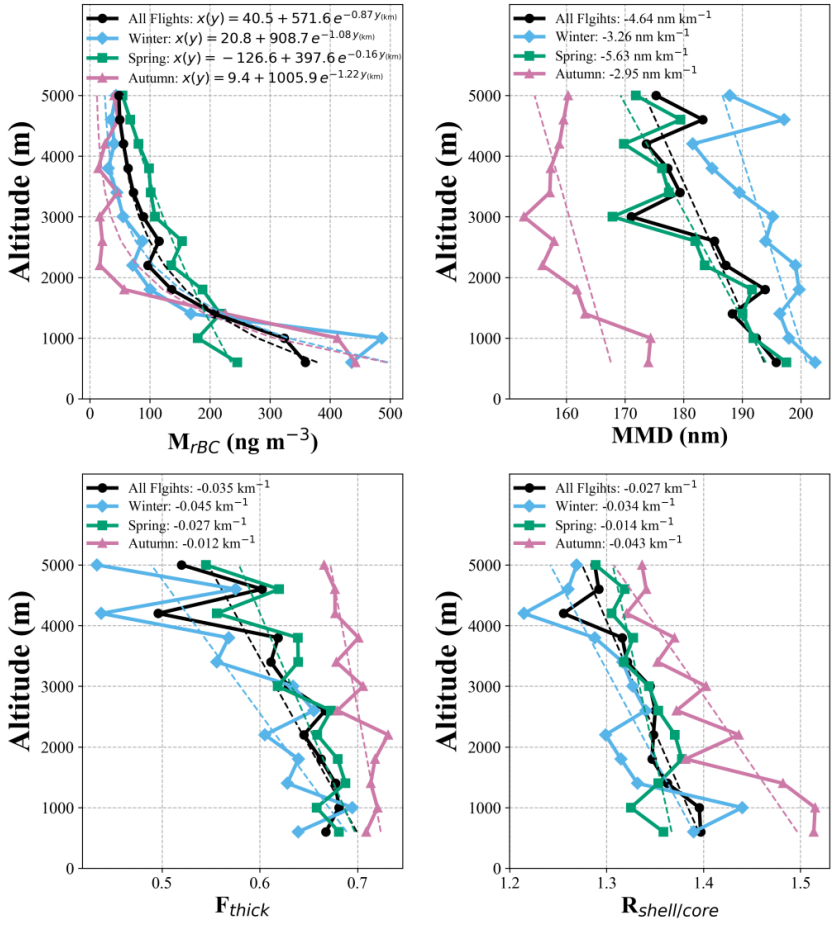

Figure 4. Seasonally varying vertical profiles of rBC particles (M_{rBC}, MMD, F_{thick}, and $R_{shell/core}$). Dashed lines show an exponential fit for M_{rBC} and linear regression fits for the others.

3.3 Distinguishing combustion source-region characteristics

The physical and chemical characteristics of combustion plumes reaching the YS were examined by analyzing rBC properties, rBC/CO ratios, and CO/CO_2 ratios in relation to air mass origin (Table 2; Fig. 5). Among the various source regions, those originating from South Korea and Japan, captured in 2021 Spring only, exhibited the smallest MMDs (163.4 nm and 168.4 nm, respectively). These MMDs are consistent with those reported for urban outflow (Cho et al., 2021; Lamb et al., 2018; McMeeking et al., 2010; Schwarz et al., 2008), suggesting a dominant influence of urban fossil-combustion emissions. In addition to smaller rBC particle sizes, South Korea- and Japan-sourced air masses also exhibited relatively low rBC/CO slopes, recorded at 0.67 ± 0.02 ng m^{-3} ppbv^{-1} and 1.11 ± 0.03 ng m^{-3} ppbv^{-1}, respectively. The rBC/CO ratio primarily reflects differences in BC/CO emission ratios across

https://doi.org/10.5194/egusphere-2025-3403
Preprint. Discussion started: 7 August 2025

combustion sources, while also capturing the effects of removal processes during atmospheric transport (Kanaya et al., 2016; Oshima et al., 2012). The particularly low rBC/CO values for these air masses likely indicate a greater contribution from gasoline combustion, which emits less rBC relative to CO compared to diesel combustion.

Table 2. Summary of rBC properties (M_{rBC}, MMD, F_{thick}, and $R_{shell/core}$) and APT for each Major Region.

	M_{rBC} (ng m^{-3})	MMD (nm)	F_{thick}	$R_{shell/core}$	APT (mm)
South Korea[a]	142.1±106.0	163.4	0.65±0.04	1.39±0.05	1.77±1.51
North Korea[b]	87.4±70.6	201.3	0.71±0.10	1.31±0.08	1.03±0.79
Japan[c]	102.6±75.0	168.4	0.68±0.04	1.40±0.05	0.56±0.83
China	351.4±287.7	194.3	0.67±0.13	1.40±0.13	0.50±1.19
Mongolia	260.1±218.9	185.3	0.63±0.14	1.38±0.12	0.95±1.28
Russia	150.4±106.7	196.9	0.60±0.15	1.35±0.10	2.11±3.54
LRT	78.5±122.0	181.5	0.48±0.21	1.26±0.14	2.89±4.51
Ocean	102.6±106.5	187.7	0.68±0.11	1.33±0.12	1.30±2.60

[a, c] 2021 Spring data only.
[b] Mostly 2022 Spring data (89%)

https://doi.org/10.5194/egusphere-2025-3403
Preprint. Discussion started: 7 August 2025

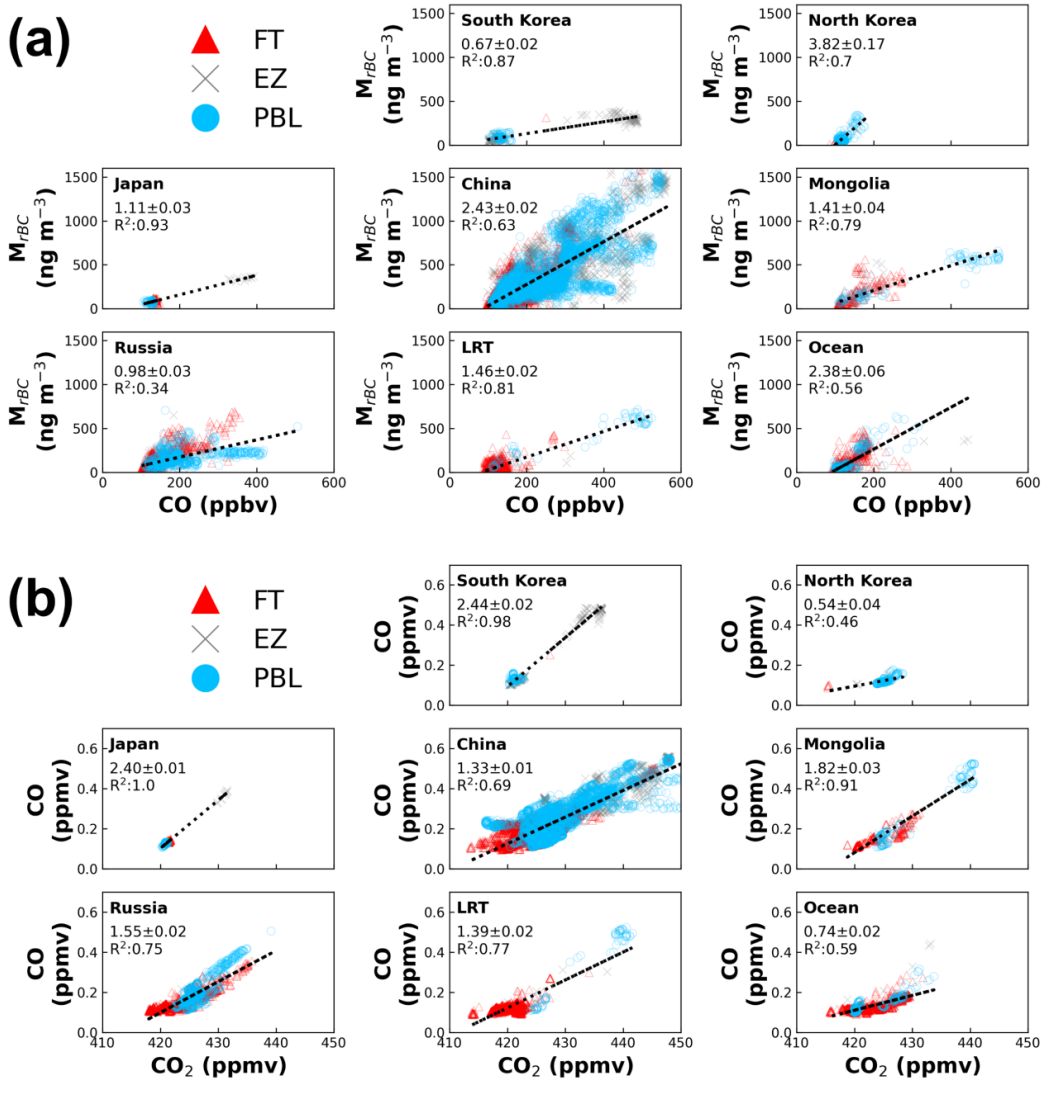

Figure 5. Linear relationships of (a) rBC mass concentration (M_{rBC}) versus CO and (b) CO versus CO_2 in each Major Region, calculated from 10-second averaged data. Sampling layers are denoted by free troposphere (FT) in red triangles, entrainment zone (EZ) in gray crosses, and planetary boundary layer (PBL) in blue circles. The black dashed lines indicate the best-fit linear regressions to all altitude data in each region; the annotated slope and coefficient of determination (R^2) quantify the strength and magnitude of each relationship.

https://doi.org/10.5194/egusphere-2025-3403
Preprint. Discussion started: 7 August 2025

Air masses originating from 'North Korea', observed exclusively during spring 2022, exhibited the highest rBC/CO slope (3.82 ± 0.17 ng m^{-3} $ppbv^{-1}$, R^2 = 0.70). It was closely aligned with the springtime KORUS-AQ campaign value (3.2 ± 0.2 ng m^{-3} $ppbv^{-1}$, R^2 = 0.83; Lamb et al., 2018) for North Korean outflow. In both studies, these slopes were the highest among all regions. Interestingly, this North Korea-sourced air showed the largest MMD (201.3 nm) and F_{thick} (0.71 ± 0.10), whereas the mean M_{rBC} (87.4 ± 70.6 ng m^{-3}) was the second lowest following 'LRT' (78.5 ± 122.0 ng m^{-3}). Given the short transport time to the YS (24 ± 26 hours) due to North Korea's geographic proximity, the largest MMD and rBC/CO slope are more likely attributable to combustion activities associated with biomass and low-graded coal rather than particle coagulation effect during transport. The mean coating thickness (30.1 ± 6.5 nm) was the second thinnest after that in LRT air masses (26.0 ± 11.5 nm), suggesting limited atmospheric processing. Despite relatively high F_{thick}, the $R_{shell/core}$ ratio remained moderate (1.31 ± 0.08), likely reflecting the short atmospheric residence time insufficient for substantial coating development.

China-sourced air exhibited distinct features in rBC properties and tracer characteristics. The rBC/CO slope was 2.43 ± 0.02 ng m^{-3} $ppbv^{-1}$ (R^2 = 0.63), in strong agreement with values reported during the KORUS-AQ campaign (2.2 ± 0.0 ng m^{-3} $ppbv^{-1}$, R^2 = 0.82; Lamb et al., 2018). Correspondingly, these air masses exhibited elevated levels of MMD (194.3 nm), F_{thick} (0.67 ± 0.13), $R_{shell/core}$ (1.40 ± 0.13) as well as M_{rBC} (351.4 ± 287.7 ng m^{-3}). Regionally, air from eastern China exhibited the highest M_{rBC} (442.5 ± 359.2 ng m^{-3}), MMD (199.3 nm), and $R_{shell/core}$ (1.43 ± 0.14), while the lowest M_{rBC} (115.8 ± 102.9 ng m^{-3}) and MMD (181.1 nm) were found in air masses from less populated northwestern China. The CO/CO_2 slope for 'China' air was substantially higher (3.33 %) than 'Korean Peninsula' (0.95 %) during the KORUS-AQ (Halliday et al., 2016). However, in this study, the CO/CO_2 slope for China air was 1.33 ± 0.01 %, which were similar to those in LRT (1.39 ± 0.02 %), Russia (1.55 ± 0.02 %), Mongolia (1.82 ± 0.03 %). This relatively lower CO/CO_2 slope in this study may reflect rapidly decreasing CO emissions in China (Yan et al., 2025; Zhao et al., 2024).

Air masses originating from Mongolia, Russia, and LRT consistently delivered larger rBC particles to the YS. Despite these air masses often experiencing the large amount of precipitation along their trajectories (APT in Table 2), the persistence of large rBC particle sizes—indicated by sustained high MMD values—suggests that the dominant sources were biomass and coal combustion, which typically emit larger rBC particles. Given that rBC particles within the accumulation mode are generally vulnerable to removal by precipitation (Lim et al., 2017), this observation highlights the robustness of source signatures even after long-range transport.

Both Mongolia- and LRT-sourced air masses were characterized by similar rBC/CO (1.41 ± 0.04 ng m^{-3} $ppbv^{-1}$ and 1.46 ± 0.02 ng m^{-3} $ppbv^{-1}$, respectively) and CO/CO_2 (1.82 ± 0.03 % and 1.39 ± 0.02 %, respectively) slopes. Compared with China-sourced air masses, the lower rBC/CO slopes suggest that these air masses had undergone more significant atmospheric aging during transport, while the relatively higher CO/CO_2 slopes imply a stronger influence of incomplete combustion. Further supporting the aging interpretation, the BC/CO emission ratio for Mongolia is reported as 14.9 ng m^{-3} $ppbv^{-1}$ in EDGAR v8.1 (Table S5; Crippa et al., 2024), indicative of strong fresh biomass burning emissions at the source. The substantially lower rBC/CO slope measured in this study (1.41 ± 0.04 ng m^{-3} $ppbv^{-1}$) therefore points to considerable loss of rBC during transport. Russian air masses exhibited clear vertical contrasts. When reaching the PBL over the YS, they exhibited lower rBC/CO slopes and higher CO/CO_2 slopes,

https://doi.org/10.5194/egusphere-2025-3403
Preprint. Discussion started: 7 August 2025

whereas the opposite pattern was observed when they arrived at FT. This vertical difference appears to be associated with elevated CO concentrations in the PBL, potentially influenced by enhanced emissions along the Russian transport pathway.

3.4 Wet removal of BC and transport efficiency

The BC/CO emission ratios reported for source regions in EDGAR v8.1 (i.e., BC emission divided by CO emission in inventories) were significantly higher than the rBC/CO slopes observed over the YS (Table S5). While the inventory-based tracer ratio reflects source-specific emission characteristics, the observed slope represents the transported air mass. This discrepancy primarily indicates preferential wet removal of rBC relative to CO during transport, assuming similar travel times from the emission source regions.

To evaluate how precipitation influences rBC characteristics remaining in the atmosphere, Table 3 presents rBC properties and the rBC/CO slope across different APT bins. All rBC-related parameters generally declined with increasing APT. Most notably, M_{rBC} decreased by more than 50 % at APT ≥ 1 mm relative to dry conditions (APT = 0), accompanied by a substantial reduction in the rBC/CO slope. Although F_{thick} declined by over 10 % at APT ≥ 1 mm relative to dry condition (APT = 0), $R_{shell/core}$ exhibited only a minor reduction (~3 %). This implies that water-soluble coating materials are not linearly scavenged by the amount of precipitation, but more complex mechanisms likely govern the wet removal efficiency such as variations in coating composition, size, and the effect of rBC core morphology.

MMD initially decreased up to APT ≥ 1 mm but rose again to 199.7 nm at APT ≥ 10 mm. Notably, air masses with APT ≥ 10 mm predominantly originated from Russia, LRT, and Mongolia, and retained larger rBC particles despite high precipitation. Again, even in the presence of heavy precipitation, the larger rBC size indicates a substantial influence from combustion sources that can emit larger particles, such as biomass and coal burning.

Table 3. Summary of rBC-related properties (M_{rBC}, MMD, F_{thick}, $R_{shell/core}$, and rBC/CO slope) across different APT bins.

	All data	APT = 0	APT ≥ 0.1 mm	APT ≥ 1 mm	APT ≥ 10 mm
M_{rBC} (ng m^{-3})	210.7±247.6	266.6±286.1	161.5±195.2	114.8±130.4	46.8±68.2
MMD (nm)	192.4	193.9	189.8	187.4	199.7
F_{thick}	0.63±0.16	0.65±0.17	0.61±0.16	0.58±0.17	0.55±0.22
$R_{shell/core}$	1.35±0.14	1.37±0.14	1.34±0.13	1.32±0.13	1.33±0.21
rBC/CO slope (ng m^{-3} ppbv^{-1})	2.25	2.40	1.96	1.43	1.15

To quantify the wet removal efficiency of rBC, its transport efficiency (TE) was estimated based on the rBC/CO slope under different APT conditions, following the approach of Matsui et al. (2011) and Oshima et al. (2012).

$$Transport\ Efficiency\ (TE) = \frac{[rBC/CO]_{APT>0}}{[rBC/CO]_{APT=0}}, \quad (1)$$

https://doi.org/10.5194/egusphere-2025-3403
Preprint. Discussion started: 7 August 2025

By definition, TE is set to 1 at APT = 0. APT was divided into 10 bins, and for each bin, the rBC/CO slope was calculated and normalized by the slope at APT = 0. $[rBC/CO]_{APT=0}$ was determined to be 2.40 ng m^{-3} $ppbv^{-1}$. Figure 6 shows the TE as a function of the APT. The blue dashed lines indicate TE values of 1/e and 0.5, and they were fitted with a stretched exponential decay (SED) function, yielding $TE = \exp(-0.246 \times APT^{0.478})$ with a R^2 of 0.91. From the fitted curve, the BC TE was found to reduce to half ($TE_{0.5}$) at APT = 8.8 mm and reached 1/e ($TE_{1/e}$) at APT = 18.9 mm. Assuming an annual precipitation of 1253.7 mm for Seosan (a coastal site near the YS), it was estimated that rBC would decrease to half and to 1/e over 2.6 days (61.3 hours) and 5.5 days (131.9 hours), respectively. These findings are broadly consistent with earlier findings. Oshima et al. (2012) reported $TE_{0.5}$ at APT ~10 mm in the East China Sea, and Kanaya et al. (2016) found $TE_{0.5}$ and $TE_{1/e}$ at 15.0 ± 3.2 and 25.5 ± 6.1 mm, respectively, in Fukue Island, Japan. Compared to these results, the slightly lower $TE_{0.5}$ and $TE_{1/e}$ thresholds observed in this study suggest a relatively faster wet removal of rBC over the YS region. This likely reflects differences in air mass characteristics, precipitation intensity, or physico-chemical BC dynamics. In particular, larger particles and those coated with highly water-soluble materials are known to be more readily scavenged, possibly contributing to the enhanced removal efficiency observed here.

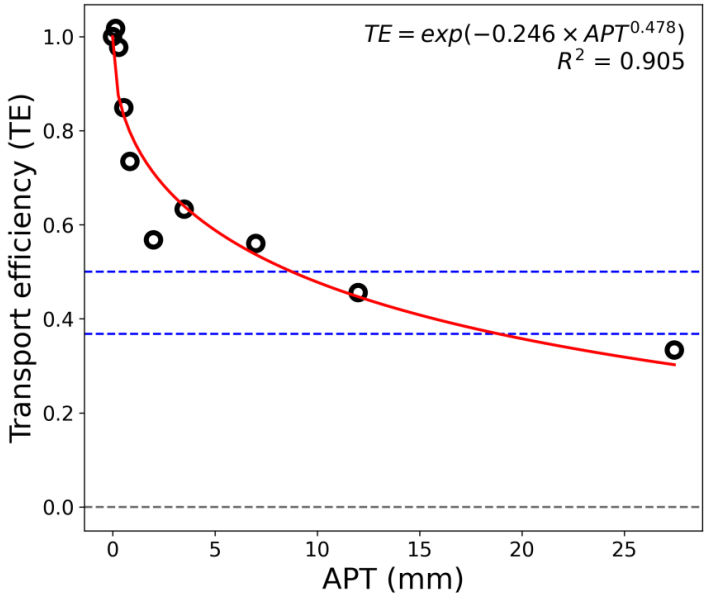

Figure 6. Transport efficiency as a function of APT observed over the YS. The blue dashed lines indicate TE values of 1/e and 0.5, respectively.

https://doi.org/10.5194/egusphere-2025-3403
Preprint. Discussion started: 7 August 2025

4 Conclusion

To investigate the physical properties of rBC and associated tracer characteristics in continental outflow, a total of 23 research flights were conducted over the YS between 8 February 2021 and 2 May 2022. Individual flight-mean M_{rBC} ranged from 58.8 to 671.1 ng m^{-3}, varying by more than an order of magnitude, with MMD of 158.6–206.6 nm, F_{thick} of 0.31–0.81, and $R_{shell/core}$ of 1.23–1.55. Notably low levels of M_{rBC} and internal mixing in 2021 Winter likely resulted from reduced anthropogenic combustion activities during the COVID-19 pandemic.

Seasonally, M_{rBC} and MMD exhibited similar trends, and vertically, M_{rBC} varied by up to two orders of magnitude between the sea surface and 5 km asl., highlighting the strong stratification in BC mass loading. Although Lamb et al. (2018) reported smaller surface MMDs near urban areas, such reductions were not observed in this study, likely due to the exclusion of urban influences in the over-sea dataset. More importantly, the vertical patterns of MMD and mixing state parameters in our study suggest a stronger influence from wet scavenging processes during particle transport, particularly at altitudes above ~3 km.

Air masses from South Korea and Japan exhibited low MMD and rBC/CO slopes, indicating a predominant influence from vehicle emissions. In contrast, China-sourced air masses showed elevated levels of M_{rBC}, MMD, F_{thick}, and $R_{shell/core}$, suggesting additional contributions from biomass and coal combustion. The rBC/CO slope of China (2.43 ± 0.02 ng m^{-3} $ppbv^{-1}$) closely matched the value observed during the KORUS-AQ campaign (2.2 ± 0.0 ng m^{-3} $ppbv^{-1}$; lamb et al., 2018), while the lower CO/CO_2 ratio likely reflects the continued decline in CO emissions in China. As increasing precipitation, rBC-related parameters generally decreased, with M_{rBC} reduced to one-fifth at ATP $\geq$ 10 mm. The relatively faster wet removal of rBC over the YS, which is estimated to reduce to 1/e within 5.5 days, highlights the influence of air mass characteristics, precipitation intensity, and particle properties on BC scavenging efficiency. Such estimates of BC lifetime provide essential constraints for improving wet deposition schemes in climate models.

In this study, our findings demonstrate rBC physical properties and tracer ratios are effective tools for distinguishing and monitoring major combustion activities from multiple countries as they retain their original information. At the same time, rBC concentrations and physical properties exhibited clear vertical and seasonal patterns, while multifaceted mixing state points to greater diversity in particle-level properties and complexity of atmospheric processing. To better constrain the atmospheric fate and climate effects of rBC, future research should focus on resolving the chemical and morphological properties of rBC particles and related atmospheric processes.

https://doi.org/10.5194/egusphere-2025-3403
Preprint. Discussion started: 7 August 2025

Code/Date availability

The data of this paper can be obtained from https://doi.org/10.5281/zenodo.15951968.

Author contributions

NY and SL designed the methodology, performed the validation, and wrote the original draft. NY also carried out data curation, formal analysis, visualization, and prepared the figures. SL supervised the project, secured funding, managed project administration, and provided resources. HJY, SO, YC, SRL, and SK contributed to manuscript review and editing. Additionally, HJY, SO, SRL, and SK provided resources and contributed to the investigation, while YC supported the methodology and formal analysis. HJY and SK also contributed to funding acquisition. All authors participated in interpreting the results and approved the final manuscript.

Competing interests

The authors declare that none of the authors has any competing interest.

Acknowledgements

We acknowledge the NOAA Air Resources Laboratory (ARL) for providing the HYSPLIT transport and dispersion model. We also acknowledge the use of black carbon emission inventory data from the Emissions Database for Global Atmospheric Research (EDGAR). In addition, we acknowledge the use of aerosol optical depth (AOD) data from NASA's MODIS (Moderate Resolution Imaging Spectroradiometer) instrument.

Financial support

This work was supported by the Korea Meteorological Administration Research and Development Program "Development of Asian dust and haze monitoring and prediction technology (KMA 2018-00521)", the National Research Foundation of Korea (NRF) from the Ministry of Science and ICT (NRF-2021R1C1C2011543 & RS-2023-00218203), and Korea Ministry of Environment (Korea MOE) as Waste to energy recycling Human resource development Project.

https://doi.org/10.5194/egusphere-2025-3403
Preprint. Discussion started: 7 August 2025

References

Berberich, J., Jacoby, S. A., Michailoudi, G., Schwarz, J. P., Viciani, S., D'Amato, F., Bianchini, G., Barucci, M., Campos, T., Ullman, K., Podolske, J. R., Gurganus, C., Smith, W. P., Ueyama, R., Honomichl, S. B., Pan, L. L., Woods, S., Wienzierl, B., Dollner, M., and Perring, A. E.: Black Carbon Reflects Extremely Efficient Aerosol Wet Removal in Monsoonal Convective Transport, J. Geophys. Res. Atmos., 130, e2024JD042692, https://doi.org/10.1029/2024JD042692, 2025.

Bond, T. C., Streets, D. G., Yarber, K. F., Nelson, S. M., Woo, J.-H., and Klimont, Z.: A technology-based global inventory of black and organic carbon emissions from combustion, J. Geophys. Res. Atmos., 109, https://doi.org/10.1029/2003JD003697, 2004.

Bond, T. C., Doherty, S. J., Fahey, D. W., Forster, P. M., Berntsen, T., DeAngelo, B. J., Flanner, M. G., Ghan, S., Kärcher, B., Koch, D., Kinne, S., Kondo, Y., Quinn, P. K., Sarofim, M. C., Schultz, M. G., Schulz, M., Venkataraman, C., Zhang, H., Zhang, S., Bellouin, N., Guttikunda, S. K., Hopke, P. K., Jacobson, M. Z., Kaiser, J. W., Klimont, Z., Lohmann, U., Schwarz, J. P., Shindell, D., Storelvmo, T., Warren, S. G., and Zender, C. S.: Bounding the role of black carbon in the climate system: A scientific assessment, J. Geophys. Res. Atmos., 118, 5380-5552, https://doi.org/10.1002/jgrd.50171, 2013.

Brooks, J., Liu, D., Allan, J. D., Williams, P. I., Haywood, J., Highwood, E. J., Kompalli, S. K., Babu, S. S., Satheesh, S. K., Turner, A. G., and Coe, H.: Black carbon physical and optical properties across northern India during pre-monsoon and monsoon seasons, Atmos. Chem. Phys., 19, 13079-13096, https://doi.org/10.5194/acp-19-13079-2019, 2019.

Cho, C., Schwarz, J. P., Perring, A. E., Lamb, K. D., Kondo, Y., Park, J.-U., Park, D.-H., Shim, K., Park, J.-S., Park, R. J., Lee, M., Song, C.-K., and Kim, S.-W.: Light-absorption enhancement of black carbon in the Asian outflow inferred from airborne SP2 and in-situ measurements during KORUS-AQ, Sci. Total Environ., 773, 145531, https://doi.org/10.1016/j.scitotenv.2021.145531, 2021.

Choi, Y., Ghim, Y. S., Zhang, Y., Park, S.-M., and Song, I.-h.: Estimation of Surface Concentrations of Black Carbon from Long-Term Measurements at Aeronet Sites over Korea, Remote Sens., 12, 3904, https://doi.org/10.3390/rs12233904, 2020a.

Choi, Y., Kanaya, Y., Takigawa, M., Zhu, C., Park, S. M., Matsuki, A., Sadanaga, Y., Kim, S. W., Pan, X., and Pisso, I.: Investigation of the wet removal rate of black carbon in East Asia: validation of a below- and in-cloud wet removal scheme in FLEXible PARTicle (FLEXPART) model v10.4, Atmos. Chem. Phys., 20, 13655-13670, https://doi.org/10.5194/acp-20-13655-2020, 2020b.

Crippa, M., Guizzardi, D., Pagani, F., Schiavina, M., Melchiorri, M., Pisoni, E., Graziosi, F., Muntean, M., Maes, J., Dijkstra, L., Van Damme, M., Clarisse, L., and Coheur, P.: Insights into the spatial distribution of global, national, and subnational greenhouse gas emissions in the Emissions Database for Global Atmospheric Research (EDGAR v8.0), Earth Syst. Sci. Data, 16, 2811-2830, https://doi.org/10.5194/essd-16-2811-2024, 2024.

Deng, H., Ji, Z., Kang, S., Zhang, Q., Cong, Z., and Dong, W.: Sustained dominance of South Asia's black carbon

https://doi.org/10.5194/egusphere-2025-3403
Preprint. Discussion started: 7 August 2025

pollution impacting the Tibetan plateau in the 21st century, npj Clim. Atmos. Sci., 7, 313, https://doi.org/10.1038/s41612-024-00856-2, 2024.

Draxler, R. R. and Hess, G. D.: Description of the HYSPLIT_4 modeling system. NOAA Tech. Memo. ERL ARL-224, 24, Aerosol Sci. Technol., 1997.

Draxler, R. R. and Hess, G. D.: An overview of the HYSPLIT_4 modeling system for trajectories, dispersion, and deposition, Aust. Meteor. Mag., 47, 295-308, 1998.

Eckhardt, S., Pisso, I., Evangeliou, N., Zwaaftink, C. G., Plach, A., McConnell, J. R., Sigl, M., Ruppel, M., Zdanowicz, C., Lim, S., Chellman, N., Opel, T., Meyer, H., Steffensen, J. P., Schwikowski, M., and Stohl, A.: Revised historical Northern Hemisphere black carbon emissions based on inverse modeling of ice core records, Nat. Commun., 14, 271, https://doi.org/10.1038/s41467-022-35660-0, 2023.

Fuller, K. A., Malm, W. C., and Kreidenweis, S. M.: Effects of mixing on extinction by carbonaceous particles, J. Geophys. Res. Atmos., 104, 15941-15954, https://doi.org/10.1029/1998JD100069, 1999.

Gandham, H., Dasari, H. P., Karumuri, A., Ravuri, P. M. K., and Hoteit, I.: Three-dimensional structure and transport pathways of dust aerosols over West Asia, npj Clim. Atmos. Sci., 5, https://doi.org/10.1038/s41612-022-00266-2, 2022.

Gao, R. S., Schwarz, J. P., Kelly, K. K., Fahey, D. W., Watts, L. A., Thompson, T. L., Spackman, J. R., Slowik, J. G., Cross, E. S., Han, J. H., Davidovits, P., Onasch, T. B., and Worsnop, D. R.: A Novel Method for Estimating Light-Scattering Properties of Soot Aerosols Using a Modified Single-Particle Soot Photometer, Aerosol Sci. Technol., 41, 125-135, https://doi.org/10.1080/02786820601118398, 2007.

Geng, F., Hua, J., Mu, Z., Peng, L., Xu, X., Chen, R., and Kan, H.: Differentiating the associations of black carbon and fine particle with daily mortality in a Chinese city, Environ. Res., 120, 27-32, https://doi.org/10.1016/j.envres.2012.08.007, 2013.

Ginot, P., Dumont, M., Lim, S., Patris, N., Taupin, J. D., Wagnon, P., Gilbert, A., Arnaud, Y., Marinoni, A., Bonasoni, P., and Laj, P.: A 10 year record of black carbon and dust from a Mera Peak ice core (Nepal): variability and potential impact on melting of Himalayan glaciers, The Cryosphere, 8, 1479-1496, https://doi.org/10.5194/tc-8-1479-2014, 2014.

Girach, I. A., Nair, V. S., Babu, S. S., and Nair, P. R.: Black carbon and carbon monoxide over Bay of Bengal during W_ICARB: Source characteristics, Atmos. Environ., 94, 508-517, https://doi.org/10.1016/j.atmosenv.2014.05.054, 2014.

Gong, X., Zhang, C., Chen, H., Nizkorodov, S. A., Chen, J., and Yang, X.: Size distribution and mixing state of black carbon particles during a heavy air pollution episode in Shanghai, Atmos. Chem. Phys., 16, 5399-5411, https://doi.org/10.5194/acp-16-5399-2016, 2016.

Gysel, M., Laborde, M., Olfert, J. S., Subramanian, R., and Gröhn, A. J.: Effective density of Aquadag and fullerene soot black carbon reference materials used for SP2 calibration, Atmos. Meas. Tech., 4, 2851-2858, https://doi.org/10.5194/amt-4-2851-2011, 2011.

Halliday, H. S., Thompson, A. M., Wisthaler, A., Blake, D. R., Hornbrook, R. S., Mikoviny, T., Müller, M., Eichler, P., Apel, E. C., and Hills, A. J.: Atmospheric benzene observations from oil and gas production in the Denver-

https://doi.org/10.5194/egusphere-2025-3403
Preprint. Discussion started: 7 August 2025

Julesburg Basin in July and August 2014, J. Geophys. Res. Atmos., 121, 11,055-011,074, https://doi.org/10.1002/2016JD025327, 2016.

Halliday, H. S., DiGangi, J. P., Choi, Y., Diskin, G. S., Pusede, S. E., Rana, M., Nowak, J. B., Knote, C., Ren, X., He, H., Dickerson, R. R., and Li, Z.: Using Short-Term CO/CO2 Ratios to Assess Air Mass Differences Over the Korean Peninsula During KORUS-AQ, J. Geophys. Res. Atmos., 124, 10951-10972, https://doi.org/10.1029/2018JD029697, 2019.

Heffter, J. L.: Air Resources Laboratories atmospheric transport and dispersion model (ARL-ATAD), National Oceanic and Atmospheric Administration (NOAA), Silver Spring, MD (United States), United States, Medium: ED; Size: 31 p., 10.2172/5015173, 1980.

Hvidtfeldt, U. A., Sørensen, M., Geels, C., Ketzel, M., Khan, J., Tjønneland, A., Overvad, K., Brandt, J., and Raaschou-Nielsen, O.: Long-term residential exposure to PM2.5, PM10, black carbon, NO2, and ozone and mortality in a Danish cohort, Environ. Int., 123, 265-272, https://doi.org/10.1016/j.envint.2018.12.010, 2019.

IPCC, 2021: Summary for Policymakers. In: Climate Change 2021: The Physical Science Basis. Contribution of Working Group I to the Sixth Assessment Report of the Intergovernmental Panel on Climate Change [Masson-Delmotte, V., P. Zhai, A. Pirani, S.L. Connors, C. Péan, S. Berger, N. Caud, Y. Chen, L. Goldfarb, M.I. Gomis, M. Huang, K. Leitzell, E. Lonnoy, J.B.R. Matthews, T.K. Maycock, T. Waterfield, O. Yelekçi, R. Yu, and B. Zhou (eds.)]. Cambridge University Press, Cambridge, United Kingdom and New York, NY, USA, pp. 3−32, doi:10.1017/9781009157896.001.

Jacobson, M. Z.: Effects of biomass burning on climate, accounting for heat and moisture fluxes, black and brown carbon, and cloud absorption effects, J. Geophys. Res. Atmos., 119, 8980-9002, https://doi.org/10.1002/2014JD021861, 2014.

Kanaya, Y., Pan, X., Miyakawa, T., Komazaki, Y., Taketani, F., Uno, I., and Kondo, Y.: Long-term observations of black carbon mass concentrations at Fukue Island, western Japan, during 2009–2015: constraining wet removal rates and emission strengths from East Asia, Atmos. Chem. Phys., 16, 10689-10705, https://doi.org/10.5194/acp-16-10689-2016, 2016.

Kanaya, Y., Yamaji, K., Miyakawa, T., Taketani, F., Zhu, C., Choi, Y., Komazaki, Y., Ikeda, K., Kondo, Y., and Klimont, Z.: Rapid reduction in black carbon emissions from China: evidence from 2009–2019 observations on Fukue Island, Japan, Atmos. Chem. Phys., 20, 6339-6356, https://doi.org/10.5194/acp-20-6339-2020, 2020.

Kang, Y., Lim, S., Lee, M., and Yoo, H. J.: Vertical Distributions of Refractory Black Carbon over the Yellow Sea during the Spring 2020, J. Korean Soc. Atmos. Environ., 37, 710-728, https://doi.org/10.5572/KOSAE.2021.37.5.710, 2021.

Kirrane, E. F., Luben, T. J., Benson, A., Owens, E. O., Sacks, J. D., Dutton, S. J., Madden, M., and Nichols, J. L.: A systematic review of cardiovascular responses associated with ambient black carbon and fine particulate matter, Environ. Int., 127, 305-316, https://doi.org/10.1016/j.envint.2019.02.027, 2019.

Klimont, Z., Kupiainen, K., Heyes, C., Purohit, P., Cofala, J., Rafaj, P., Borken-Kleefeld, J., and Schöpp, W.: Global anthropogenic emissions of particulate matter including black carbon, Atmos. Chem. Phys., 17, 8681-8723, https://doi.org/10.5194/acp-17-8681-2017, 2017.

https://doi.org/10.5194/egusphere-2025-3403
Preprint. Discussion started: 7 August 2025

610 Ko, J., Krasowsky, T., and Ban-Weiss, G.: Measurements to determine the mixing state of black carbon emitted from
611 the 2017-2018 California wildfires and urban Los Angeles, Atmos. Chem. Phys., 20, 15635-15664,
612 https://doi.org/10.5194/acp-20-15635-2020, 2020.
613 Kompalli, S. K., Babu, S. N. S., Moorthy, K. K., Satheesh, S. K., Gogoi, M. M., Nair, V. S., Jayachandran, V. N., Liu,
614 D., Flynn, M. J., and Coe, H.: Mixing state of refractory black carbon aerosol in the South Asian outflow over
615 the northern Indian Ocean during winter, Atmos. Chem. Phys., 21, 9173-9199, https://doi.org/10.5194/acp-21-
616 9173-2021, 2021.
617 Kompalli, S. K., Suresh Babu, S. N., Satheesh, S. K., Krishna Moorthy, K., Das, T., Boopathy, R., Liu, D., Darbyshire,
618 E., Allan, J. D., Brooks, J., Flynn, M. J., and Coe, H.: Seasonal contrast in size distributions and mixing state
619 of black carbon and its association with PM1.0 chemical composition from the eastern coast of India, Atmos.
620 Chem. Phys., 20, 3965-3985, https://doi.org/10.5194/acp-20-3965-2020, 2020.
621 Kondo, Y., Moteki, N., Oshima, N., Ohata, S., Koike, M., Shibano, Y., Takegawa, N., and Kita, K.: Effects of wet
622 deposition on the abundance and size distribution of black carbon in East Asia, J. Geophys. Res. Atmos., 121,
623 4691-4712, https://doi.org/10.1002/2015JD024479, 2016.
624 Krasowsky, T. S., McMeeking, G. R., Wang, D., Sioutas, C., and Ban-Weiss, G. A.: Measurements of the impact of
625 atmospheric aging on physical and optical properties of ambient black carbon particles in Los Angeles, Atmos.
626 Environ., 142, 496-504, https://doi.org/10.1016/j.atmosenv.2016.08.010, 2016.
627 Kurokawa, J. and Ohara, T.: Long-term historical trends in air pollutant emissions in Asia: Regional Emission
628 inventory in ASia (REAS) version 3, Atmos. Chem. Phys., 20, 12761-12793, https://doi.org/10.5194/acp-20-
629 12761-2020, 2020.
630 Kuwata, M., Kondo, Y., and Takegawa, N.: Critical condensed mass for activation of black carbon as cloud
631 condensation nuclei in Tokyo, J. Geophys. Res. Atmos., 114, https://doi.org/10.1029/2009JD012086, 2009.
632 Kuwata, M., Kondo, Y., Miyazaki, Y., Komazaki, Y., Kim, J. H., Yum, S. S., Tanimoto, H., and Matsueda, H.: Cloud
633 condensation nuclei activity at Jeju Island, Korea in spring 2005, Atmos. Chem. Phys., 8, 2933-2948,
634 https://doi.org/10.5194/acp-8-2933-2008, 2008.
635 Laborde, M., Mertes, P., Zieger, P., Dommen, J., Baltensperger, U., and Gysel, M.: Sensitivity of the Single Particle
636 Soot Photometer to different black carbon types, Atmos. Meas. Tech., 5, 1031-1043,
637 https://doi.org/10.5194/amt-5-1031-2012, 2012.
638 Laborde, M., Crippa, M., Tritscher, T., Jurányi, Z., Decarlo, P. F., Temime-Roussel, B., Marchand, N., Eckhardt, S.,
639 Stohl, A., Baltensperger, U., Prévôt, A. S. H., Weingartner, E., and Gysel, M.: Black carbon physical properties
640 and mixing state in the European megacity Paris, Atmos. Chem. Phys., 13, 5831-5856,
641 https://doi.org/10.5194/acp-13-5831-2013, 2013.
642 Lack, D. A., Cappa, C. D., Cross, E. S., Massoli, P., Ahern, A. T., Davidovits, P., and Onasch, T. B.: Absorption
643 Enhancement of Coated Absorbing Aerosols: Validation of the Photo-Acoustic Technique for Measuring the
644 Enhancement, Aerosol Sci. Technol., 43, 1006-1012, https://doi.org/10.1080/02786820903117932, 2009.
645 Lamb, K. D., Perring, A. E., Samset, B., Peterson, D., Davis, S., Anderson, B. E., Beyersdorf, A., Blake, D. R.,
646 Campuzano-Jost, P., Corr, C. A., Diskin, G. S., Kondo, Y., Moteki, N., Nault, B. A., Oh, J., Park, M., Pusede,

https://doi.org/10.5194/egusphere-2025-3403
Preprint. Discussion started: 7 August 2025

S. E., Simpson, I. J., Thornhill, K. L., Wisthaler, A., and Schwarz, J. P.: Estimating Source Region Influences on Black Carbon Abundance, Microphysics, and Radiative Effect Observed Over South Korea, J. Geophys. Res. Atmos., 123, 13,527-513,548, https://doi.org/10.1029/2018JD029257, 2018.

Lim, S., Lee, M., and Yoo, H. J.: Size distributions, mixing state, and morphology of refractory black carbon in an urban atmosphere of northeast Asia during summer, Sci. Total Environ., 856, https://doi.org/10.1016/j.scitotenv.2022.158436, 2023.

Lim, S., Faïn, X., Ginot, P., Mikhalenko, V., Kutuzov, S., Paris, J. D., Kozachek, A., and Laj, P.: Black carbon variability since preindustrial times in the eastern part of Europe reconstructed from Mt. Elbrus, Caucasus, ice cores, Atmos. Chem. Phys., 17, 3489-3505, https://doi.org/10.5194/acp-17-3489-2017, 2017.

Lim, S., Lee, M., Laj, P., Kim, S.-W., Ahn, K.-H., Gil, J., Shang, X., Zanatta, M., and Kang, K.-S.: Regional characteristics of fine aerosol mass increase elucidated from long-term observations and KORUS-AQ campaign at a Northeast Asian background site, Elem. Sci. Anthropocene, 10, 10.1525/elementa.2022.00020, 2022.

Liu, D., Allan, J. D., Young, D. E., Coe, H., Beddows, D., Fleming, Z. L., Flynn, M. J., Gallagher, M. W., Harrison, R. M., Lee, J., Prevot, A. S. H., Taylor, J. W., Yin, J., Williams, P. I., and Zotter, P.: Size distribution, mixing state and source apportionment of black carbon aerosol in London during wintertime, Atmos. Chem. Phys., 14, 10061-10084, https://doi.org/10.5194/acp-14-10061-2014, 2014.

Liu, D., Joshi, R., Wang, J., Yu, C., Allan, J. D., Coe, H., Flynn, M. J., Xie, C., Lee, J., Squires, F., Kotthaus, S., Grimmond, S., Ge, X., Sun, Y., and Fu, P.: Contrasting physical properties of black carbon in urban Beijing between winter and summer, Atmos. Chem. Phys., 19, 6749-6769, https://doi.org/10.5194/acp-19-6749-2019, 2019.

Liu, D., Flynn, M., Gysel, M., Targino, A., Crawford, I., Bower, K., Choularton, T., Jurányi, Z., Steinbacher, M., Hüglin, C., Curtius, J., Kampus, M., Petzold, A., Weingartner, E., Baltensperger, U., and Coe, H.: Single particle characterization of black carbon aerosols at a tropospheric alpine site in Switzerland, Atmos. Chem. Phys., 10, 7389-7407, https://doi.org/10.5194/acp-10-7389-2010, 2010.

Liu, H., Pan, X., Liu, D., Liu, X., Chen, X., Tian, Y., Sun, Y., Fu, P., and Wang, Z.: Mixing characteristics of refractory black carbon aerosols at an urban site in Beijing, Atmos. Chem. Phys., 20, 5771-5785, https://doi.org/10.5194/acp-20-5771-2020, 2020.

Liu, H., Pan, X., Lei, S., Zhang, Y., Du, A., Yao, W., Tang, G., Wang, T., Xin, J., Li, J., Sun, Y., Cao, J., and Wang, Z.: Vertical distribution of black carbon and its mixing state in the urban boundary layer in summer, Atmos. Chem. Phys., 23, 7225-7239, https://doi.org/10.5194/acp-23-7225-2023, 2023.

Liu, H., Pan, X., Wang, D., Liu, X., Tian, Y., Yao, W., Lei, S., Zhang, Y., Li, J., Lei, L., Xie, C., Fu, P., Sun, Y., and Wang, Z.: Mixing characteristics of black carbon aerosols in a coastal city using the CPMA-SP2 system, Atmos. Res., 265, 105867, https://doi.org/10.1016/j.atmosres.2021.105867, 2022.

Liu, S., Aiken, A. C., Gorkowski, K., Dubey, M. K., Cappa, C. D., Williams, L. R., Herndon, S. C., Massoli, P., Fortner, E. C., Chhabra, P. S., Brooks, W. A., Onasch, T. B., Jayne, J. T., Worsnop, D. R., China, S., Sharma, N., Mazzoleni, C., Xu, L., Ng, N. L., Liu, D., Allan, J. D., Lee, J. D., Fleming, Z. L., Mohr, C., Zotter, P., Szidat,

https://doi.org/10.5194/egusphere-2025-3403
Preprint. Discussion started: 7 August 2025

S., and Prévôt, A. S. H.: Enhanced light absorption by mixed source black and brown carbon particles in UK winter, Nat. Commun., 6, 8435, https://doi.org/10.1038/ncomms9435, 2015.

Lund, M. T., Samset, B. H., Skeie, R. B., Watson-Parris, D., Katich, J. M., Schwarz, J. P., and Weinzierl, B.: Short Black Carbon lifetime inferred from a global set of aircraft observations, npj Clim. Atmos. Sci., 1, https://doi.org/10.1038/s41612-018-0040-x, 2018.

Matsui, H., Kondo, Y., Moteki, N., Takegawa, N., Sahu, L. K., Zhao, Y., Fuelberg, H. E., Sessions, W. R., Diskin, G., Blake, D. R., Wisthaler, A., and Koike, M.: Seasonal variation of the transport of black carbon aerosol from the Asian continent to the Arctic during the ARCTAS aircraft campaign, J. Geophys. Res. Atmos., 116, https://doi.org/10.1029/2010JD015067, 2011.

McMeeking, G. R., Hamburger, T., Liu, D., Flynn, M., Morgan, W. T., Northway, M., Highwood, E. J., Krejci, R., Allan, J. D., Minikin, A., and Coe, H.: Black carbon measurements in the boundary layer over western and northern Europe, Atmos. Chem. Phys., 10, 9393-9414, https://doi.org/10.5194/acp-10-9393-2010, 2010.

Metcalf, A. R., Craven, J. S., Ensberg, J. J., Brioude, J., Angevine, W., Sorooshian, A., Duong, H. T., Jonsson, H. H., Flagan, R. C., and Seinfeld, J. H.: Black carbon aerosol over the Los Angeles Basin during CalNex, J. Geophys. Res. Atmos., 117, https://doi.org/10.1029/2011JD017255, 2012.

Moteki, N. and Kondo, Y.: Effects of Mixing State on Black Carbon Measurements by Laser-Induced Incandescence, Aerosol Sci. Technol., 41, 398-417, 10.1080/02786820701199728, 2007.

Moteki, N. and Kondo, Y.: Dependence of Laser-Induced Incandescence on Physical Properties of Black Carbon Aerosols: Measurements and Theoretical Interpretation, Aerosol Sci. Technol., 44, 663-675, https://doi.org/10.1080/02786826.2010.484450, 2010.

Moteki, N., Kondo, Y., and Nakamura, S.-i.: Method to measure refractive indices of small nonspherical particles: Application to black carbon particles, J. Aerosol Sci., 41, 513-521, https://doi.org/10.1016/j.jaerosci.2010.02.013, 2010.

Ohata, S., Mori, T., Kondo, Y., Sharma, S., Hyvärinen, A., Andrews, E., Tunved, P., Asmi, E., Backman, J., Servomaa, H., Veber, D., Eleftheriadis, K., Vratolis, S., Krejci, R., Zieger, P., Koike, M., Kanaya, Y., Yoshida, A., Moteki, N., Zhao, Y., Tobo, Y., Matsushita, J., and Oshima, N.: Estimates of mass absorption cross sections of black carbon for filter-based absorption photometers in the Arctic, Atmos. Meas. Tech., 14, 6723-6748, https://doi.org/10.5194/amt-14-6723-2021, 2021.

Oshima, N., Kondo, Y., Moteki, N., Takegawa, N., Koike, M., Kita, K., Matsui, H., Kajino, M., Nakamura, H., Jung, J. S., and Kim, Y. J.: Wet removal of black carbon in Asian outflow: Aerosol Radiative Forcing in East Asia (A-FORCE) aircraft campaign, J. Geophys. Res. Atmos., 117, https://doi.org/10.1029/2011JD016552, 2012.

Peischl, J., Ryerson, T. B., Holloway, J. S., Parrish, D. D., Trainer, M., Frost, G. J., Aikin, K. C., Brown, S. S., Dubé, W. P., Stark, H., and Fehsenfeld, F. C.: A top-down analysis of emissions from selected Texas power plants during TexAQS 2000 and 2006, J. Geophys. Res. Atmos., 115, https://doi.org/10.1029/2009JD013527, 2010.

Petzold, A., Ogren, J. A., Fiebig, M., Laj, P., Li, S. M., Baltensperger, U., Holzer-Popp, T., Kinne, S., Pappalardo, G., Sugimoto, N., Wehrli, C., Wiedensohler, A., and Zhang, X. Y.: Recommendations for reporting "black carbon" measurements, Atmos. Chem. Phys., 13, 8365-8379, https://doi.org/10.5194/acp-13-8365-2013, 2013.

https://doi.org/10.5194/egusphere-2025-3403
Preprint. Discussion started: 7 August 2025

Riemer, N., West, M., Zaveri, R., and Easter, R.: Estimating black carbon aging time-scales with a particle-resolved aerosol model, J. Aerosol Sci., 41, 143-158, https://doi.org/10.1016/j.jaerosci.2009.08.009, 2010.

Schwarz, J. P., Spackman, J. R., Gao, R. S., Perring, A. E., Cross, E., Onasch, T. B., Ahern, A., Wrobel, W., Davidovits, P., Olfert, J., Dubey, M. K., Mazzoleni, C., and Fahey, D. W.: The Detection Efficiency of the Single Particle Soot Photometer, Aerosol Sci. Technol., 44, 612-628, https://doi.org/10.1080/02786826.2010.481298, 2010.

Schwarz, J. P., Gao, R. S., Spackman, J. R., Watts, L. A., Thomson, D. S., Fahey, D. W., Ryerson, T. B., Peischl, J., Holloway, J. S., Trainer, M., Frost, G. J., Baynard, T., Lack, D. A., de Gouw, J. A., Warneke, C., and Del Negro, L. A.: Measurement of the mixing state, mass, and optical size of individual black carbon particles in urban and biomass burning emissions, Geophys. Res. Lett., 35, https://doi.org/10.1029/2008GL033968, 2008.

Steffen, W., Rockström, J., Richardson, K., Lenton, T. M., Folke, C., Liverman, D., Summerhayes, C. P., Barnosky, A. D., Cornell, S. E., Crucifix, M., Donges, J. F., Fetzer, I., Lade, S. J., Scheffer, M., Winkelmann, R., and Schellnhuber, H. J.: Trajectories of the Earth System in the Anthropocene, Proc. Natl. Acad. Sci. U.S.A., 115, 8252-8259, https://doi.org/10.1073/pnas.1810141115, 2018.

Stein, A. F., Draxler, R. R., Rolph, G. D., Stunder, B. J. B., Cohen, M. D., and Ngan, F.: NOAA's HYSPLIT Atmospheric Transport and Dispersion Modeling System, Bull. Am. Meteorol. Soc., 96, 2059-2077, https://doi.org/10.1175/BAMS-D-14-00110.1, 2015.

Stephens, M., Turner, N., and Sandberg, J.: Particle identification by laser-induced incandescence in a solid-state laser cavity, Appl. Opt., 42, 3726-3736, https://doi.org/10.1364/AO.42.003726, 2003.

Suntharalingam, P., Jacob, D. J., Palmer, P. I., Logan, J. A., Yantosca, R. M., Xiao, Y., Evans, M. J., Streets, D. G., Vay, S. L., and Sachse, G. W.: Improved quantification of Chinese carbon fluxes using CO2/CO correlations in Asian outflow, J. Geophys. Res. Atmos., 109, https://doi.org/10.1029/2003JD004362, 2004.

Taylor, J. W., Allan, J. D., Liu, D., Flynn, M., Weber, R., Zhang, X., Lefer, B. L., Grossberg, N., Flynn, J., and Coe, H.: Assessment of the sensitivity of core / shell parameters derived using the single-particle soot photometer to density and refractive index, Atmos. Meas. Tech., 8, 1701-1718, https://doi.org/10.5194/amt-8-1701-2015, 2015.

Utavong, T., Thongyen, T., Bualert, S., Choomanee, P., Kongkeaw, S., Rattanapotanan, T., Phupijit, J., Maneejantra, S., and Changplaiy, N.: Influence of Relative Humidity and Aging on Morphology and Chemical Composition on Biomass Burning Particle, Aerosol Air Qual. Res., 24, 230234, https://doi.org/10.4209/aaqr.230234, 2024.

Wang, Q., Huang, R. J., Cao, J., Han, Y., Wang, G., Li, G., Wang, Y., Dai, W., Zhang, R., and Zhou, Y.: Mixing State of Black Carbon Aerosol in a Heavily Polluted Urban Area of China: Implications for Light Absorption Enhancement, Aerosol Sci. Technol., 48, 689-697, https://doi.org/10.1080/02786826.2014.917758, 2014.

Wang, Y., Munger, J. W., Xu, S., McElroy, M. B., Hao, J., Nielsen, C. P., and Ma, H.: CO₂ and its correlation with CO at a rural site near Beijing: implications for combustion efficiency in China, Atmos. Chem. Phys., 10, 8881-8897, https://doi.org/10.5194/acp-10-8881-2010, 2010.

Weingartner, E., Burtscher, H., and Baltensperger, U.: Hygroscopic properties of carbon and diesel soot particles, Atmos. Environ., 31, 2311-2327, https://doi.org/10.1016/S1352-2310(97)00023-X, 1997.

Wu, Y., Zhang, R., Tian, P., Tao, J., Hsu, S. C., Yan, P., Wang, Q., Cao, J., Zhang, X., and Xia, X.: Effect of ambient

https://doi.org/10.5194/egusphere-2025-3403
Preprint. Discussion started: 7 August 2025

humidity on the light absorption amplification of black carbon in Beijing during January 2013, Atmos. Environ., 124, 217-223, https://doi.org/10.1016/j.atmosenv.2015.04.041, 2016.

Wu, Y., Xia, Y., Zhou, C., Tian, P., Tao, J., Huang, R.-J., Liu, D., Wang, X., Xia, X., Han, Z., and Zhang, R.: Effect of source variation on the size and mixing state of black carbon aerosol in urban Beijing from 2013 to 2019: Implication on light absorption, Environ. Pollut., 270, 116089, https://doi.org/10.1016/j.envpol.2020.116089, 2021.

Yan, Q., Xiao, T., Zhang, W., Kong, S., Zhang, Y., Gao, Q., Shu, Y., Li, H., and Wang, H.: Long term emission and simulation on air quality from residential coal burning in China, Environ. Res. Commun., 7, 021006, https://doi.org/10.1088/2515-7620/adb241, 2025.

Yang, X., Ji, D., Li, J., He, J., Gong, C., Xu, X., Wang, Z., Liu, Y., Bi, F., Zhang, Z., and Chen, Y.: Impacts of springtime biomass burning in Southeast Asia on atmospheric carbonaceous components over the Beibu Gulf in China: Insights from aircraft observations, Sci. Total Environ., 857, https://doi.org/10.1016/j.scitotenv.2022.159232, 2023.

Zhang, Y., Sperber, K. R., and Boyle, J. S.: Climatology and Interannual Variation of the East Asian Winter Monsoon: Results from the 1979–95 NCEP/NCAR Reanalysis, Mon. Weather Rev., 125, 2605-2619, https://doi.org/10.1175/1520-0493(1997)125<2605:CAIVOT>2.0.CO;2, 1997.

Zhao, D., Huang, M., Tian, P., He, H., Lowe, D., Zhou, W., Sheng, J., Wang, F., Bi, K., Kong, S., Yang, Y., Liu, Q., Liu, D., and Ding, D.: Vertical characteristics of black carbon physical properties over Beijing region in warm and cold seasons, Atmos. Environ., 213, 296-310, https://doi.org/10.1016/j.atmosenv.2019.06.007, 2019.

Zhao, G., Tan, T., Hu, S., Du, Z., Shang, D., Wu, Z., Guo, S., Zheng, J., Zhu, W., Li, M., Zeng, L., and Hu, M.: Mixing state of black carbon at different atmospheres in north and southwest China, Atmos. Chem. Phys., 22, 10861-10873, https://doi.org/10.5194/acp-22-10861-2022, 2022.

Zhao, J., Chen, H., Qi, X., Chi, X., Jia, M., Jiang, F., Zhong, S., Zheng, B., and Ding, A.: Observed decade-long improvement of combustion efficiency in the Yangtze River Delta region in China, Environ. Res. Lett., 19, 074001, https://doi.org/10.1088/1748-9326/ad521e, 2024.

Zhao, P., Dong, F., Yang, Y., He, D., Zhao, X., Zhang, W., Yao, Q., and Liu, H.: Characteristics of carbonaceous aerosol in the region of Beijing, Tianjin, and Hebei, China, Atmos. Environ., 71, 389-398, https://doi.org/10.1016/j.atmosenv.2013.02.010, 2013.

Zhou, X., Gao, J., Wang, T., Wu, W., and Wang, W.: Measurement of black carbon aerosols near two Chinese megacities and the implications for improving emission inventories, Atmos. Environ., 43, 3918-3924, https://doi.org/10.1016/j.atmosenv.2009.04.062, 2009.

Zuberi, B., Johnson, K. S., Aleks, G. K., Molina, L. T., Molina, M. J., and Laskin, A.: Hydrophilic properties of aged soot, Geophys. Res. Lett., 32, https://doi.org/10.1029/2004GL021496, 2005.